Adaptively Selecting Interferograms for SBAS-InSAR Based on Graph Theory and Turbulence Atmosphere

MENG DUAN[1], BING XU[ID][1], ZHI-WEI LI[ID][1], WEN-HAO WU[2], JIAN-CHAO WEI[2], YUN-MENG CAO[3], AND JI-HONG LIU[1]

[1]School of Geoscience and Info-Physics Engineering, Central South University, Changsha 410083, China
[2]Hunan Province Key Laboratory of Coal Resources Clean-utilization and Mine Environment Protection, Hunan University of Science and Technology, Xiangtan 411105, China
[3]Physical Science and Engineering Division, King Abdullah University of Science and Technology, Thuwal 23955, Saudi Arabia

Corresponding authors: Bing Xu (xubing@csu.edu.cn) and Zhi-Wei Li (zwli@csu.edu.cn)

ABSTRACT The spatial-temporal baseline threshold method is commonly used to select interferograms for the Small BAseline Subset interferometric synthetic aperture radar (SBAS-InSAR) technique. However, this selection strategy is rather empirical and prone to including highly contaminated interferograms or excluding those with high quality. To overcome these limitations, this study first derives the relationship between the measurement accuracy of unknown parameters and the number of selected interferograms with their corresponding qualities. Subsequently, an adaptive interferogram selection method is proposed on the basis of Graph Theory (GT) and the turbulence atmospheric effects of interferogram. This proposed method first identifies and deletes the SAR image that is severely polluted by atmospheric phase. Second, high-quality interferograms are selected for SBAS-InSAR based on their corresponding turbulence atmospheric variance. Compared with the traditional selection method, this approach can significantly reduce the effect of turbulence atmosphere on SBAS-InSAR. A set of simulated experiments and real Sentinel-1A data in Hawaii, United States, validate the good performance of the proposed method.

INDEX TERMS SBAS-InSAR, graph theory, turbulence atmosphere, interferogram network, variance and covariance matrix.

I. INTRODUCTION

Since its proposal, the classical Small BAseline Subset interferometric synthetic aperture radar (SBAS-InSAR) has been proven as an important and powerful geodetic tool for obtaining non-differential water vapor in time series [1]–[3], recovering digital elevation maps (DEM) [4], and monitoring ground deformations caused by earthquake, volcanic, landslides, permafrost, man-made construction, groundwater extraction, underground oil and mining [5]–[11]. Subsequently, SBAS is successfully extended to other forms, including Parallel SBAS (P-SBAS) [12], Multidimensional SBAS (M-SBAS) [13], New SBAS (N-SBAS) [14], and Intermittent SBAS (I-SBAS) [15] to meet various study areas and data conditions. Notably, all these time series InSAR (TS-InSAR) techniques are based on an appropriate combination of interferograms produced from time series SAR images gathered at different time epochs over the same area of interest. As each SAR image inevitably contains noises (e.g., atmospheric noise), interferograms contain varying degrees of noise, including atmosphere, decorrelation noise, co-registration noise and data processing noise [16]. However, estimating and completely separating these errors from interferograms is difficult under most circumstances [16]–[20]. Therefore, the main limitation of each interferogram is its noises, especially atmosphere and decorrelation noise, caused by temporal and spatial variations of water vapor in the atmosphere and ground reflectivity, respectively. Meanwhile, the quality of interferograms involved in direct calculation affects the accuracy of the SBAS-InSAR measurement.

Furthermore, with satellite development, especially Sentinel-1A/B satellites, that reduce the revisit time to six days, the number of SAR images and interferograms is increasing [21], a phenomenon described as Big Data [22]. The increased availability of SAR images and

The associate editor coordinating the review of this manuscript and approving it for publication was Jenny Mahoney.

interferograms unprecedentedly facilitate the application of SBAS-InSAR technique. However, the big data of remote sensing datasets increase the complexity and difficulty in selecting high-quality interferogram (i.e., the interferogram that contains little turbulence atmosphere and other noise) in the short time for SBAS-InSAR measurement. Moreover, the adaptively selected interferogram is one of the key steps in implementing an automated SBAS-InSAR system for engineering applications.

At present, the commonly used method is setting the spatial-temporal baseline thresholds to select interferograms [23], which is clearly simple and convenient to implement. However, the combination of SLC images and the number of interferograms both depend on the predefined spatial-temporal baseline thresholds, which are always determined on the basis of experience of the study area. In addition, this method only considers the spatial-temporal baseline as the standard rather than the quality of interferograms. Thus, poor-quality interferograms with short spatial-temporal baseline can be selected for SBAS-InSAR measurement and high-quality interferograms may be discarded due to the spatial-temporal baseline exceeding the thresholds. To solve these limitations in this traditional method, this study proposes an adaptive optimization interferogram selection method via Graph Theory (GT) and turbulence atmospheric variance of all available interferograms. This method can avoid pre-defining the spatial-temporal baseline threshold by a complete combination of all SLC images. Moreover, the measurement accuracy of SBAS-InSAR improves by identifying and preventing the SLC images and interferograms that are severely polluted by turbulence atmospheric noise. The main steps of the proposed method are as follows:

1. Find the relationship between the measurement accuracy of unknown parameters (e.g. surface deformation) and the number and quality of selected interferograms in SBAS-InSAR using theoretical derivation;
2. Generate all possible interferograms from all SAR images;
3. Calculate the turbulence atmospheric variance of each SLC image and discard the SAR image with clearly large variance and simultaneously remove its corresponding interferograms;
4. Apply the GT algorithm to the remaining interferograms to obtain the minimum spanning tree (MST) interferograms and ensure the connectivity of SBAS-InSAR;
5. Calculate the mean value of the variance of the remaining interferograms and delete those with variance larger than the mean value to guarantee the measurement accuracy.

The proposed approach is successfully applied to a set of simulated experiments and real experiments at Hawaii island. The rest of this paper is structured as follows. In Section II, the relationship between the unknown parameters and the selected interferograms in SBAS-InSAR are derived and the main steps of the innovative algorithm are analyzed in depth. Section III and Section IV then applies the proposed method to the simulated and real experiments, respectively, followed

by discussions in Section V. Finally, conclusions are drawn in Section VI.

II. ADAPTIVELY SELECTION METHOD OF INTERFEROGRAM
A. DERIVATION OF THE RELATIONSHIP BETWEEN THE UNKNOWN PARAMETERS AND THE SELECTED INTERFEROGRAMS IN SBAS-InSAR

In this study, N SAR images are assumed to be connected to M interferograms and M equals to $\frac{N(N-1)}{2}$ under the condition of a complete combination from all SAR images. According to the standard differential InSAR (D-InSAR), the differential phase $\left(\Delta\varphi_{ifg}^{o,i,j}\right)$ of pixel o in an interferogram with master acquisition t_i and slave acquisition t_j can be written as [24], [25]:

$$\Delta\varphi_{ifg}^{o,i,j} = \Delta\varphi_{defo}^{o,i,j} + \Delta\varphi_{topo}^{o,i,j} + \Delta\varphi_{orb}^{o,i,j} + \Delta\varphi_{atm}^{o,i,j} + \Delta\varphi_{dec}^{o,i,j} \quad (1)$$

where o is the *oth* pixel in the SAR image. i and j are the *ith* and *jth* index of the SAR image, respectively. $\Delta\varphi_{defo}^{o,i,j}$ is the surface deformation between two SAR acquisitions. $\Delta\varphi_{topo}^{o,i,j}$ is the topography phase and can be compensated by an external DEM. $\Delta\varphi_{orb}^{o,i,j}$ is the general orbit error that can be modeled as a surface trend and then separated from the interferometric phase [26]. $\Delta\varphi_{atm}^{o,i,j}$ and $\Delta\varphi_{dec}^{o,i,j}$ are the atmospheric and noise phases (e.g., decorrelation noise phase), respectively. Notably, the atmospheric phase includes the vertical stratification that can be fitted by a mathematic model and the turbulence atmosphere that is difficult to estimate [24], [27]. Therefore, after removing the residual topographic phase, vertical stratification atmosphere and orbit error, Equation (1) can be written in a matrix as:

$$\boldsymbol{Y} = \boldsymbol{A}\boldsymbol{X} + \boldsymbol{e} \quad (2)$$

where $\boldsymbol{Y}$ is the $M \times 1$ differential interferometric phase vector of pixel o, $\boldsymbol{X}$ is the $N \times 1$ unknown parameter vector (i.e., surface deformation at pixel o), $\boldsymbol{e}$ is the noise that contains the atmosphere and decorrelation noise. $\boldsymbol{A}$ is the coefficient matrix with the dimension of $M \times N$ and can be written as:

$$\boldsymbol{A} = \boldsymbol{G}\boldsymbol{\tau} \quad (3)$$

where $\boldsymbol{G}$ is the incidence matrix with M rows and N columns and can be determined by the interferogram network in SBAS-InSAR. If the older SAR image is adopted as the master, matrix $\boldsymbol{G}$ then fills each row with 1 for the former epoch, -1 for the latter, and 0 for the rest (i.e., Equation (4)).

$$\boldsymbol{G} = \begin{bmatrix} 1 & -1 & 0 & 0 & \cdots & 0 & 0 \\ 1 & 0 & -1 & 0 & \cdots & 0 & 0 \\ 0 & 1 & -1 & 0 & \cdots & 0 & 0 \\ & \vdots & & & \cdots & & \vdots \\ 0 & 0 & 0 & 0 & \cdots & 1 & -1 \end{bmatrix} \quad (4)$$

$$\boldsymbol{\tau} = \begin{bmatrix} t_1 & 0 & 0 & \cdots & \cdots & 0 & 0 \\ 0 & t_2 & 0 & \cdots & \cdots & 0 & 0 \\ \vdots & & \cdots & & \cdots & & \vdots \\ 0 & 0 & 0t_i & \cdots & & 0 & 0 \\ \vdots & & \cdots & & \cdots & & \vdots \\ 0 & 0 & 0 & \cdots & \cdots & 0 & t_N \end{bmatrix} \quad (5)$$

where t_i is the time epoch of the *ith* SAR image and the dimension of $\boldsymbol{\tau}$ is $N \times N$.

According to the stochastic modeling for SBAS-InSAR, the stochastic model of the Equation (2) can be written as:

$$\boldsymbol{Q}_{YY} = \boldsymbol{Q}_{atm} + \boldsymbol{Q}_{decorr} \quad (6)$$

where $\boldsymbol{Q}_{YY}, \boldsymbol{Q}_{atm}$ and $\boldsymbol{Q}_{decorr}$ are the variance-covariance matrix of the observations, atmospheric phase and the decorrelation phase, respectively.

Combing Equations (2), (3) and (6), the unknown parameter vector $\boldsymbol{X}$ and the corresponding variance-covariance matrix $\boldsymbol{Q}_{XX}$ can be obtained by the Weighted Least-Squares (WLS) method [28].

$$\boldsymbol{X} = \left((\boldsymbol{G\tau})^T \boldsymbol{Q}_{YY}^{-1} (\boldsymbol{G\tau}) \right)^{-1} (\boldsymbol{G\tau})^T \boldsymbol{Q}_{YY}^{-1} \boldsymbol{Y} \quad (7)$$

$$\boldsymbol{Q}_{XX} = \left((\boldsymbol{G\tau})^T \boldsymbol{Q}_{YY}^{-1} (\boldsymbol{G\tau}) \right)^{-1} \quad (8)$$

Assuming isotropic and second-order intrinsic stationarity, then the turbulence atmosphere can be described by the variogram or structure function [29]. The structure function of turbulence atmosphere can be approximated using the spherical model (i.e., Equation (9)) [19]:

$$\gamma(r) = \begin{cases} c_0 + c \left(\dfrac{3r}{2a} - \dfrac{r^3}{2a^3} \right) & r \leq a \\ c_0 + c & r > a \end{cases} \quad (9)$$

where r is the variogram or structure function. r is the spatial distance. a is the largest spatial correlation distance and the so-called *range*. c_0 is the *nugget* mainly caused by the spatial variation of turbulence atmosphere in interferogram. c is the *sill* value of the model in Geostatistics, and $c_0 + c$ is commonly considered as the variance of interferogram.

The relationship of turbulence atmosphere between the K ($1 \leq K \leq M$) interferogram, which form from the *ith* and *jth* SAR images, and the corresponding SAR images can be written as:

$$\phi_{atm}^{i,j} = \varphi_{atm}^j - \varphi_{atm}^i \quad (10)$$

where ϕ and φ are the phase of turbulence atmosphere of interferogram and SLC image, respectively. Therefore, the relationship of the turbulence atmosphere between the M interferograms and N SAR images can be written as:

$$\boldsymbol{\phi}_{atm} = \boldsymbol{G}\boldsymbol{\varphi}_{atm} \quad (11)$$

where $\boldsymbol{\phi}_{atm}$ and $\boldsymbol{\varphi}_{atm}$ are the atmospheric value of the M interferograms with dimensions of $M \times 1$ and N epochs with dimensions of $N \times 1$, respectively.

Notably, the turbulence atmosphere is uncorrelated in the time domain [24]. Therefore, combining Equation (10) and the variance-covariance propagation formula, the relationship of the atmospheric variance between the M interferograms and N SAR images can be written in the matrix form as:

$$\boldsymbol{V}_{atm}(\boldsymbol{\phi}) = \boldsymbol{B}\boldsymbol{V}_{atm}(\boldsymbol{\varphi}) \quad (12)$$

where $\boldsymbol{V}_{atm}(\boldsymbol{\phi})$ and $\boldsymbol{V}_{atm}(\boldsymbol{\varphi})$ are the turbulence atmospheric variances of the M interferograms with dimensions of $M \times 1$ and N epochs with dimensions of $N \times 1$, respectively. $\boldsymbol{B}$ is the design matrix with dimensions of $M \times N$, which is determined by the matrix $\boldsymbol{G}$:

$$\boldsymbol{B} = abs(\boldsymbol{G}) = \begin{bmatrix} 1 & 1 & 0 & 0 & \cdots & 0 & 0 \\ 1 & 0 & 1 & 0 & \cdots & 0 & 0 \\ 0 & 1 & 1 & 0 & \cdots & 0 & 0 \\ \vdots & & & \cdots & & & \vdots \\ 0 & 0 & 0 & 0 & \cdots & 1 & 1 \end{bmatrix} \quad (13)$$

where $abs(\bullet)$ represents the absolute value. Combing Equations (12) and (13), the turbulence atmospheric variance in time series (i.e., $\boldsymbol{V}_{atm}(\boldsymbol{\varphi})$) can be obtained by the least-squares method, as:

$$\boldsymbol{V}_{atm}(\boldsymbol{\varphi}) = \left((abs(\boldsymbol{G}))^T (abs(\boldsymbol{G})) \right)^{-1} (abs(\boldsymbol{G}))^T \boldsymbol{V}_{atm}(\boldsymbol{\phi}) \quad (14)$$

Then, the variance and covariance matrix of turbulence atmosphere in the time domain is:

$$\boldsymbol{Q}_{atm}^{SLC} = diag(\boldsymbol{V}_{atm}(\boldsymbol{\varphi}))$$
$$= \begin{bmatrix} V_{atm}(v_1) & & & \\ & V_{atm}(v_2) & & \\ & & \ddots & \\ & & & V_{atm}(v_N) \end{bmatrix}_{N \times N} \quad (15)$$

Combining Equations (11), (14) and (15), and the variance-covariance propagation formulas, the variance-covariance matrix of the turbulence atmosphere in interferogram domain (i.e., $\boldsymbol{Q}_{atm}$ in Equation (6)) can be written as:

$$\boldsymbol{Q}_{atm} = \boldsymbol{G}\boldsymbol{Q}_{atm}^{SLC}\boldsymbol{G}^T \quad (16)$$

The decorrelation noise in SBAS-InSAR is mainly caused by temporal decorrelation, spatial decorrelation, system noise decorrelation, processing-inducing noise (e.g., coregistration and interpolation noise) and Doppler-centroid decorrelation [24], [30]. A common method for estimating the variance-covariance matrix of decorrelation noise (i.e., $\boldsymbol{Q}_{decorr}$ in Equation (6)) can be described as [31], [32]:

$$\boldsymbol{Q}_{decorr} = \frac{1 - \rho^2}{2\rho^2} \quad (17)$$

where ρ is the coherence. Combining Equations (6) (16) and (17), Equation (6) can be written as:

$$\boldsymbol{Q}_{YY} = \boldsymbol{G}\boldsymbol{Q}_{atm}^{SLC}\boldsymbol{G}^T + \frac{1 - \rho^2}{2\rho^2} \quad (18)$$

Based on Equation (18), Equations (7) and (8) can be written as:

$$X = \left((G\tau)^T \left(G\left(diag\left(V_{atm}\left(\varphi\right)\right)\right)G^T\right.\right.$$
$$\left.\left. + \frac{1-\rho^2}{2\rho^2}\right)^{-1}(G\tau)\right)^{-1}(G\tau)^T$$
$$\left(G\left(diag\left(V_{atm}\left(\varphi\right)\right)\right)G^T + \frac{1-\rho^2}{2\rho^2}\right)^{-1}Y \quad (19)$$

$$Q_{XX} = \left((G\tau)^T \left(G\left(diag\left(V_{atm}\left(\varphi\right)\right)\right)G^T\right.\right.$$
$$\left.\left. + \frac{1-\rho^2}{2\rho^2}\right)^{-1}(G\tau)\right)^{-1} \quad (20)$$

Equations (19) and (20) show that the unknown parameter vector X can be obtained. The corresponding variance-covariance matrix Q_{XX} is not only affected by the matrix G, but also the phase variance of turbulence atmosphere in each SAR image and decorrelation noise. Furthermore, the phase variance caused by decorrelation noise depends on the coherence (i.e., ρ) from Equation (17). Clearly, finding the optimal interferogram network (i.e., matrix G) is difficult for matrix X and Q_{XX} at present. For this reason, this study proposes an adaptive method to optimize the interferogram selection for SBAS-InSAR based on statistical method (e.g., the mean and standard deviation (STD) of turbulence atmospheric noise in interferograms).

B. DETECTION AND ELIMINATION OUTLIERS OF SAR IMAGES

Given that the SAR image connects interferograms and each SAR image inevitably contains noise, the outliers of SAR image largely bias the estimation. Therefore, the first step is to identify and eliminate the outliers of SAR images using the variance of turbulence atmospheric phase. The decorrelation noise (i.e., Q_{decorr}) in interferogram selection optimization is not considered for three reasons. First, no study has obtained the decorrelation variance of the entire interferogram at present. However, the proposed method is based on the variance of the entire interferogram instead of each pixel, and thus pixels are not considered to select interferograms in the discussion. Second, the contribution of Q_{decorr} is less significant than that of Q_{atm} under most circumstances in many previous studies [17]–[19]. Furthermore, according to the principle of SBAS-InSAR [23], the pixels with low coherence are rejected to decrease the effect of decorrelation noise. Third, the essence of the proposed algorithm to select interferogram is comparing the variance of entire interferogram. Thus, this study considered only the relative values of the entire interferogram variances rather than the absolute values.

As stated in Section A, the structure function of turbulence atmosphere is calculating using the spherical model (i.e., Equation (9)) and $c_0 + c$ is considered as the variance of each interferogram (i.e., $V_{atm}(\phi)$). Then, based on Equation (14), the turbulence atmospheric phase variance of each

SLC image (i.e., $V_{atm}(\varphi)$) is obtained. After calculating the mean and STD of $V_{atm}(\varphi)$, the SLC images with difference with the mean is larger than 3x the STD and their corresponding interferograms are deleted simultaneously.

C. APPLYING THE GRAPH THEORY TO ENSURE CONNECTIVITY

After eliminating the interferograms connected from the outliers of SLC images (e.g., sth SAR image), the corresponding row (e.g., sth row) of Q_{atm}^{SLC} are also deleted and the new Q_{atm}^{SLC} remarked as $Q_{atm}^{SLC-new}$. Then, the rest N_{rest} of SAR images and M_{rest} interferograms are regarded as the corresponding N_{rest} vertices and M_{rest} edges in GT [33]. To connect the N_{rest} SAR images, the inverse of turbulence atmospheric variances of each interferogram are used as the weight of the corresponding M_{rest} interferograms. Subsequently, the $N_{rest} - 1$ interferograms with smaller variances can be obtained by applying the MST algorithm in GT [34], [35]. Thus, the high-quality and least number of interferograms (i.e., $N_{rest}-1$) that connects the rest of N_{rest} SAR images can be obtained.

D. SELECTION OF REDUNDANT INTERFEROGRAMS FOR SBAS-InSAR

After obtaining the $N_{rest} - 1$ interferograms by using MST method, the final step is to select the high-quality interferogram for SBAS-InSAR from the residual interferograms. Similar to Section B, the mean of turbulence atmospheric phase variance of the residual interferograms is calculated and the interferograms with variance larger than the mean are removed. Then, the total of selected interferogram for SBAS-InSAR is the sum of the $N_{rest} - 1$ interferograms by MST and the redundant interferograms. Applications of the proposed method are shown in the following sections.

III. SYNTHETIC TEST

In this section, a set of synthetic experiments is used to test the performance of the proposed adaptive optimization interferograms for SBAS-InSAR. First, 24 independent SAR images are simulated with realistic spatial-temporal baseline distribution according to the Sentinel-1A data sets over the Los Angeles Basin, South California. Therefore, 276 interferograms are obtained by a complete combination from these SAR images. The dimensions of each simulated image is 200 × 200 pixels and a subsidence funnel with 25 mm/year velocity is simulated. Then, the turbulence atmospheric signal based on the Kolmogorov turbulence theory is simulated for each image [24]. Considering the temporal variability of turbulence atmosphere, the simulated atmosphere is multiplied by a constant randomly selected between 0 and 5 [17]. Meanwhile, four decorrelation noises (i.e., thermal decorrelation, coregistration induced decorrelation, geometric decorrelation and temporal decorrelation) are added to each interferogram [16].

After obtaining the variances of the 276 interferograms using Equation (9) (i.e., Fig. 1), the variances of the
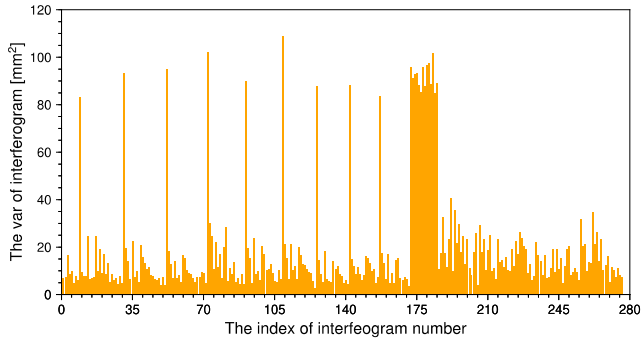
FIGURE 1. Variances of simulated 276 interferograms.

24 simulated SLC images can be obtained using Equation (14). Meanwhile, Fig. 2 compares the phase variance between the simulated and estimated 24 SLC images. Clearly, the estimated and simulated results are almost identical. Furthermore, the correlation between their variances is as high as 99.93%. These figures illustrate the reliability of the estimated phase variance.
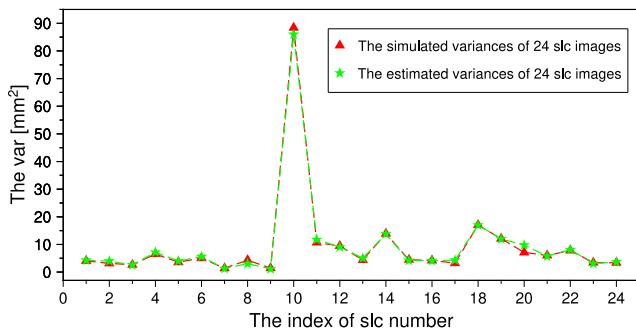

FIGURE 2. Comparison the simulated and estimated variances of 24 SLC images: Red triangles and green stars represent the simulated and estimated variances of 24 SLC images, respectively.

To better identify the low-quality SLC image (i.e., the one that is severely polluted by turbulence atmosphere), Fig. 3(a) describes the estimated phase variances of 24 SLC images by histogram. By comparison, the 10*th* image has a significantly larger variance than the others. Fig. 3(b) shows the calculations of difference of each SLC image variance and
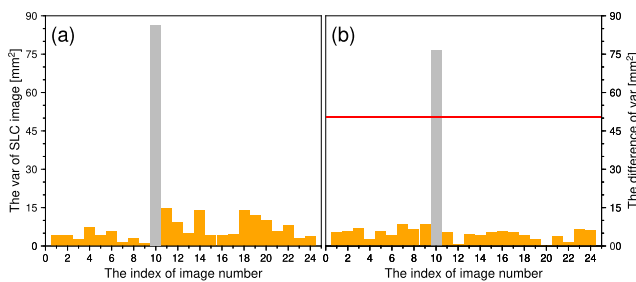

FIGURE 3. (a) Variances of simulated 24 SLC images and (b) differences between the variances of 24 SLC images and the mean variance of 24 SLC images. Red lines represent the 3x of STD.

the mean variance of 24 SLC images. The red lines represent the 3x STD of the 24 SLC image variances. Notably, only the 10*th* image has a difference that is larger than the 3x STD, and is therefore regarded as the outlier and should be deleted. Meanwhile, the interferograms connected by this image are also deleted from the total. Consequently, 23 SLC images and 253 interferograms remain.

As the turbulence atmosphere variances of the remaining 253 interferograms are known, their inverses are regarded as the weight of corresponding interferograms. As shown in Fig. 4(a), the least and optimal interferograms can be obtained using the MST method in GT. This method selects the optimal interferograms and ensures simultaneous connectivity of all remaining 23 SLC images in the time domain.
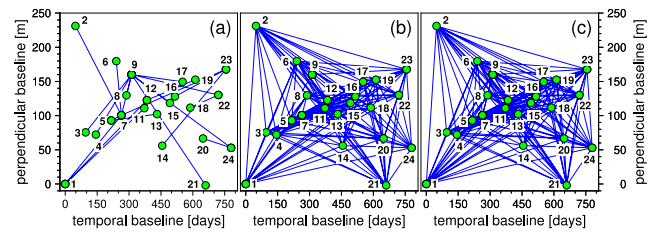

FIGURE 4. (a). Spatial structure graph of MST interferogram; (b). Selected redundant interferograms; and (c). Total interferograms for SBAS-InSAR: Green dots represent the image time epochs and edges represent the interferograms.

Given that 23 SLC images remain, then the least number of interferograms selected by the MST method is 22. The next step is to select better-quality interferograms for SBAS-InSAR from the residual 231 interferograms. No criterion guides the number of interferograms for SBAS-InSAR, and thus the mean of the residual 231 interferograms variances are simply calculated and the interferogram with variance that is smaller than the mean variance is selected. Fig. 4(b) shows the selected redundant interferograms used for SBAS-InSAR and Fig. 4(c) shows the total interferograms selected using this method, namely, the sum of Figs. 4(a) and (b). Fig. 4(c) shows that the total number of selected interferograms using this proposed method is 166.

Based on these selected interferograms and Equations (19) and (20), the estimated mean velocity is obtained in Fig. 5(a) and shows good agreement with the simulation (i.e., Fig. 5(b)). To increase clarity, Fig. 5(c) shows the difference between the estimated (i.e., Fig. 5(a)) and simulated mean velocities (i.e., Fig. 5(b)) and the Fig. 5(d) shows the corresponding histogram. Figs. 5(c) and (d) show that the difference follows a Gaussian distribution with the mean close to zero. This indicates the good performance of the estimated result from the selected interferograms.

To illustrate the deleted interferograms polluted by turbulence atmosphere, Fig. 6 shows two randomly selections from the 110 deleted interferograms. Compared with the simulated mean velocity (i.e., Fig. 5(b)), the real deformation signal is hardly identifiable due to noises in Fig. 6(a). Furthermore,
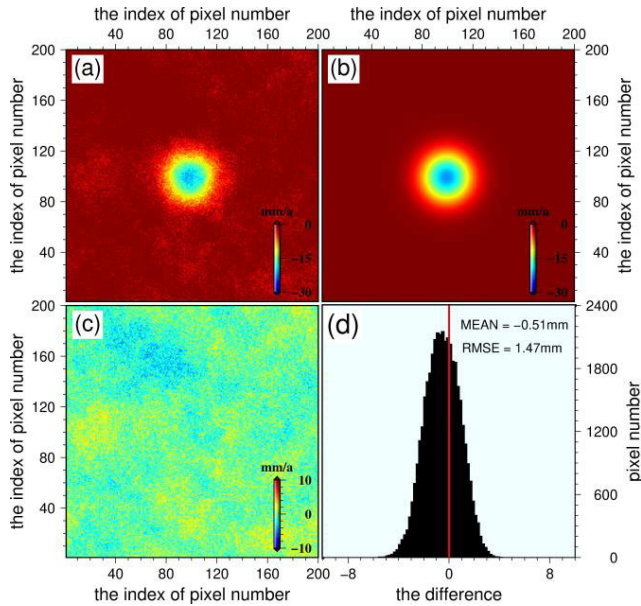
FIGURE 5. (a) Estimated and (b) simulated mean velocities; (c). Difference between the simulated and estimated mean velocities, and (d) Correspondence of the difference in (c).
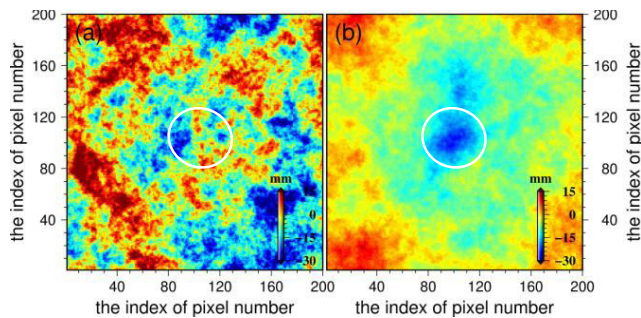
FIGURE 6. (a) Deleted interferogram formed by the 6 *th* and 10 *th* SLC images; (b). Deleted interferogram formed by the 11 *th* and 18 *th* SLC images: White circles in (a) and (b) indicate the location of displacement.

the locations of non-deformation are also clearly contaminated in Fig. 6(b).

Next, a series of experiments is carried out to compare the performance of the proposed interferogram selection method and the traditional SBAS-InSAR method, namely, the predefined temporal-spatial baseline threshold method. For simplification, the temporal and spatial baseline thresholds range 80-785 days with a step of 5 days and 80-785 m with a step of 5 m, respectively. Fig. 7 shows that the selected SLC images are 22 and 23 when the temporal-spatial baseline threshold are smaller than 95 days and 95 m, and 155 days and 155 m, respectively. In other words, the excluded SLC images are 2 and 1, respectively. This means that SLC images are excluded when the predefined temporal and spatial baseline threshold are small. Moreover, the temporal and spatial baseline threshold did not detect the outliers, namely the 10*th* image, which contains unidentified large. All of these can cause bias in SBAS-InSAR unknown parameters estimation.
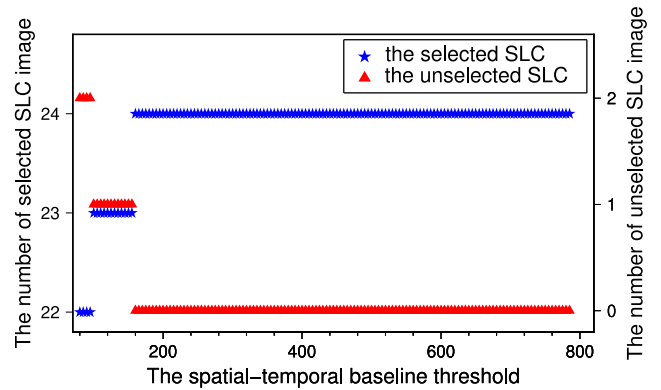
FIGURE 7. Selected (blue stars) and unselected (red dots) SLC images with varied spatial-temporal baseline thresholds.

Based on the selected SLC images, Fig. 8 describes the number of interferograms under different spatial-temporal baseline thresholds. As expected, the number of selected interferograms (i.e., blue stars) increases as the temporal-spatial baseline threshold increases. This finding helps increase the measurement accuracy of SBAS-InSAR by increasing the redundant interferograms [28]. However, the red dots described in Fig. 8(a) show that the number of interferograms with variance larger than the corresponding mean variance also increases. Meanwhile, the red triangles in Fig. 8(b), the number of unselected interferograms with variance smaller than the mean variance decreases with the increasing spatial temporal baseline thresholds. These finding indicate that the predefined spatial-temporal baseline threshold method can easily select low-quality interferograms and miss those with high quality, which reduces the accuracy of SBAS-InSAR improvement. Meanwhile, the proposed method ensures the number and quality of the selected SLC images and interferograms. Therefore, compared with the temporal-spatial baseline threshold method, the proposed method achieves an apparent mean improvement of approximately 20%, as shown in Fig. 9.
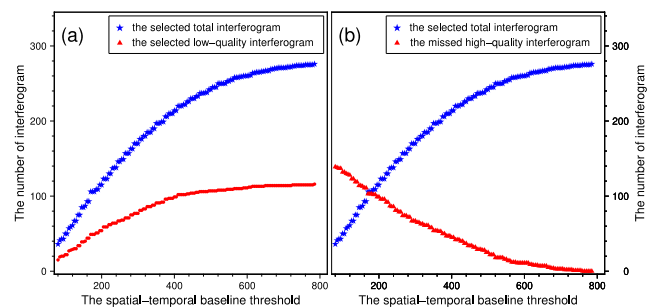

FIGURE 8. Number of interferograms under different spatial-temporal baseline thresholds; (a) Blue stars and red dots represent the selected total interferograms and the selected low-quality interferograms, respectively. (b) Blue stars and red triangles represent the selected total interferograms and missed high-quality interferograms, respectively.

IV. EXPERIMENT RESULTS
This section presents the deformation results from applying the proposed interferogram selection method in the big island of Hawaii. Data of 24 descending Sentinel-1 SAR images are
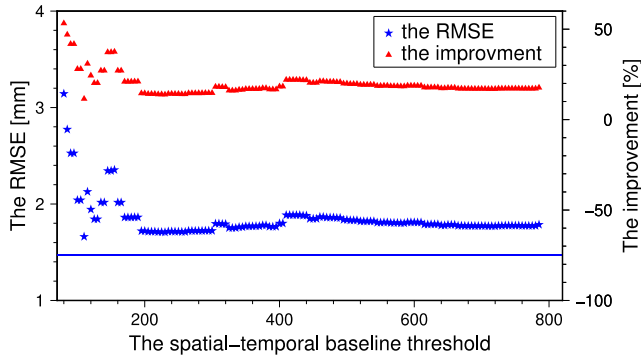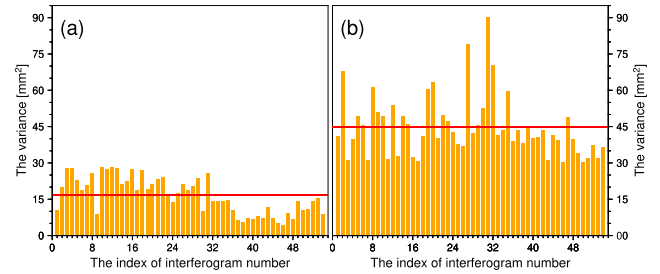
FIGURE 9. Comparison of the RMSE of the spatial-temporal baseline threshold method (blue stars) and the proposed method (blue line): Red triangles represent the efficiency improvement of the proposed method compared with the spatial-temporal baseline method.
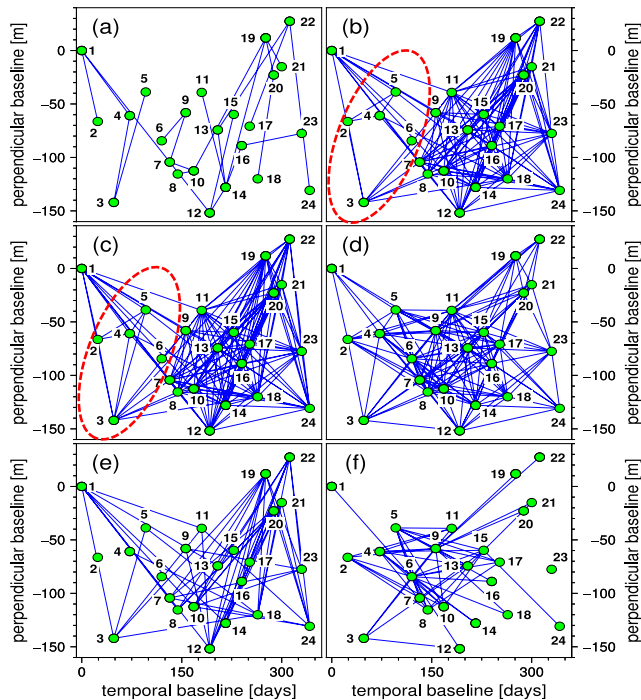

FIGURE 10. (a). Spatial structure graph of MST interferogram; (b). Selected redundant interferograms from the proposed method; (c) and (d). Total interferograms selected by the proposed method and by the traditional method, respectively. (e) 54 interferograms only selected by the proposed method and not selected by the traditional method; (f) 54 interferograms only selected by the traditional method and not selected by the proposed method: Green dots represent the image time epochs and edges represent the interferograms, respectively. Red ellipses are used to intuitively denote the difference between (b) and (c).

FIGURE 11. (a) and (b). Variances of the 54 different interferograms selected by the proposed and traditional methods, respectively: Red lines denote the mean variance for each method.
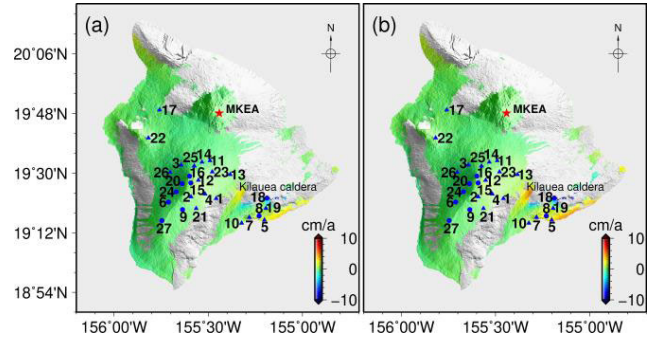

FIGURE 12. Ground deformation mean velocities in Hawaii, retrieved by the (a) proposed method and (b) the traditional method: Red stars represent the reference point (i.e., MKEA site), blue triangles represent the GPS stations validating that the proposed method outperforms the traditional method. Blue dots denote the GPS stations with RMSE larger under the proposed method than under the traditional method. The 27 GPS stations used for validation are AINP, ALAL, ALEP, ANIP, APNT, BLBP, KAON, KEAW, KHKU, KULE, MLCC, MLES, MLPR, MLRD, MLSP, MOKP, NIHO, NUPM, PG2R, PHAN, PIIK, PMAU, PUKA, SLPC, STEP, TOUO and YEEP.

acquired from 5 January 2018 to 12 December 2018. Thus, 276 interferograms can be generated from any two combined images. Each interferogram is multilooked with 20 pixels in azimuth and 4 pixels in range directions and the orbit phase is corrected by the precise orbit data. Meanwhile, we select the MKEA site as the reference point for each interferogram and the remaining 27 Global Positioning System (GPS) stations are used for validation.

After removing the topography phase by the external digital elevation model (30m) from the Shuttle Radar Topography Mission (SRTM) [35], the improved Goldstein filter and the minimum cost flow (MCF) algorithm are carried out for each interferogram [36]–[38]. Meanwhile, the vertical atmospheric phase in each interferogram is removed using a second order polynomial [27].

After obtaining the variance of each interferogram using Equation (9), the variance of each SAR image is calculated using Equation (14). The mean and STD of the 24 SLC variances are 13.56mm and 8.55mm^2, respectively. The differences between the SLC and the mean variances are all less than the 3x STD, and thus no outliers of SLC image remain. Fig. 10(a) shows the least number of interferograms (i.e., 23) to connect the 24 SAR images after applying the MST algorithm. The mean variance of the remaining 253 interferograms is 28.78mm. After deleting those with variance larger than the mean variance (i.e., 28.78mm), the redundant interferograms are selected and shown in Fig. 10(b). Therefore, the sum of Figs. 10(a) and (b), 162, is the total interferograms selected by the proposed method (i.e., Fig. 10(c)). To achieve the same number of interferograms selected by the proposed method, the traditional temporal-spatial baseline threshold was set to 160 days and 89 m, respectively. Fig. 10(d) shows
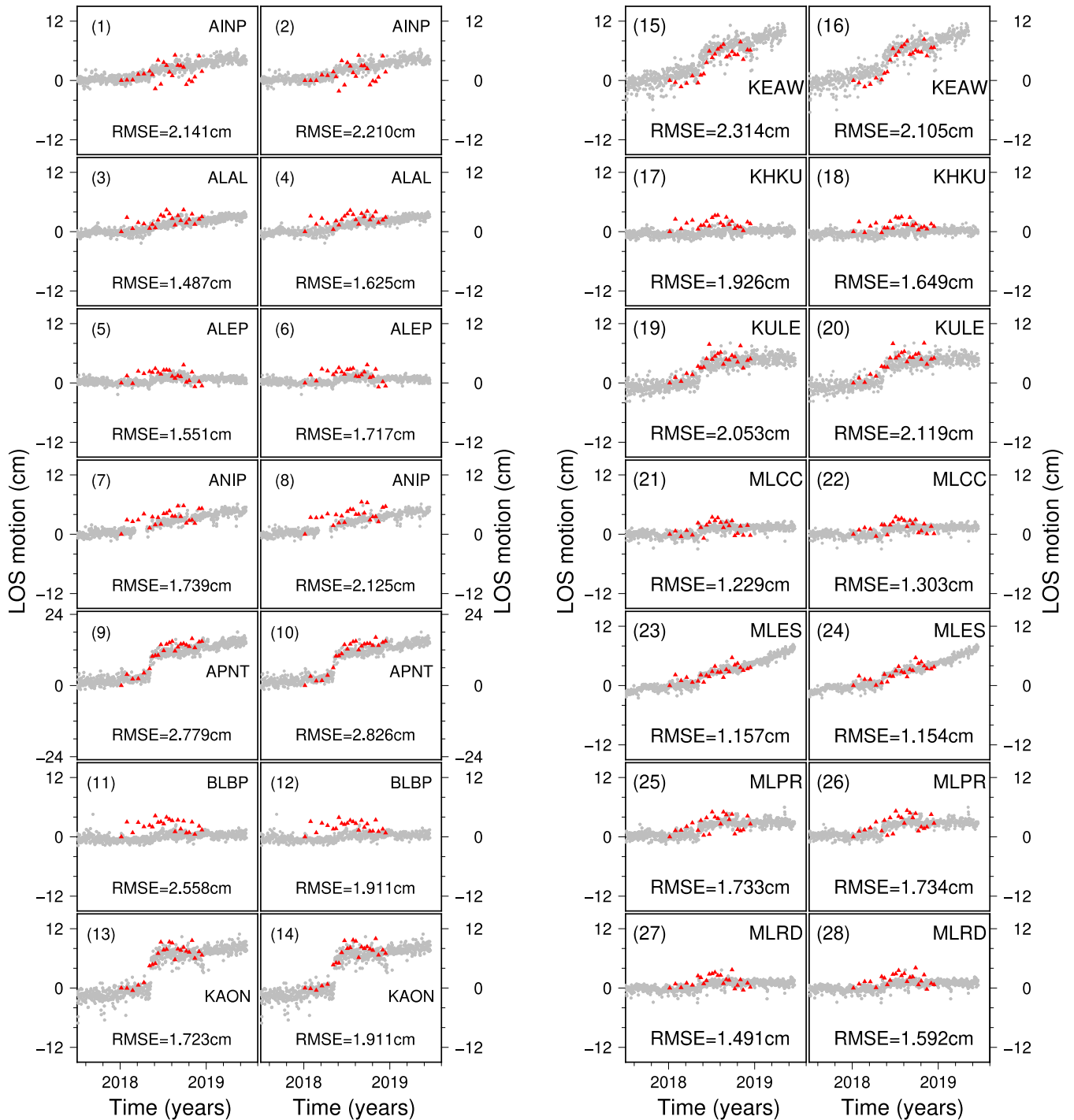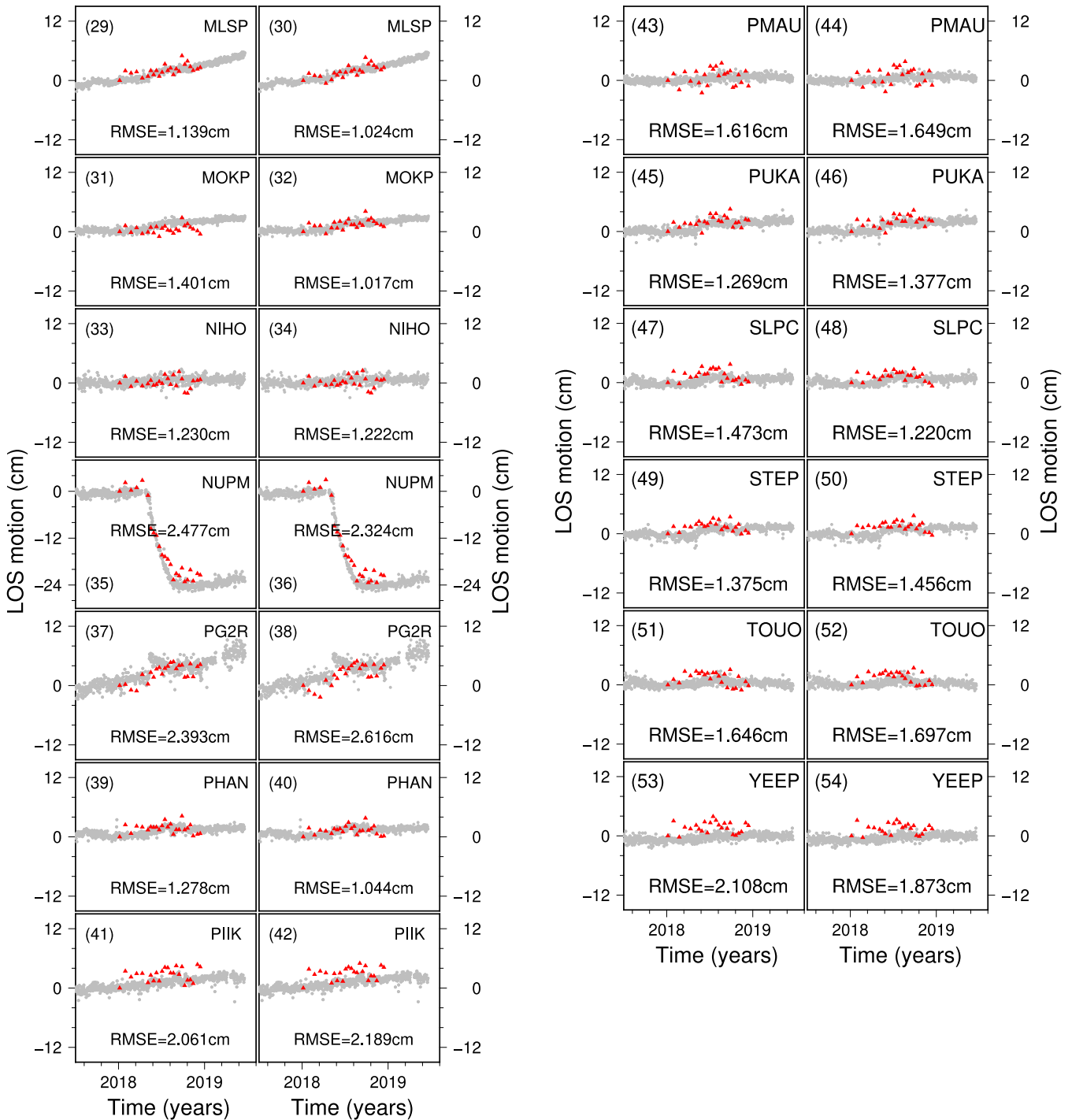
FIGURE 13. Comparison of the time series displacements of the 27 GPS stations using the proposed method (red triangles on the left) and the traditional method (red triangles on the right): Gray dots represent the corresponding GPS time series results projected on the LOS direction.

the corresponding spatial-temporal baseline distribution of the selected interferograms.

Comparing Figs. 10(c) and (d), the spatial-temporal baseline distribution quite differs between the selected interferograms from the two methods. Therefore, Figs. 10(c) and (d) have 54 different interferograms, which are clearly displayed in succeeding figures. Fig. 10(e) describes the 54 interferograms only selected by the proposed method and

not selected by the traditional method. Fig. 10(f) shows the 54 interferograms only selected by the traditional method and not selected by the proposed method. Meanwhile, Fig. 11(a) shows the variances of the 54 different interferograms selected by the proposed method with an average variance (i.e., red line) of 16.42mm. Similarly, Fig. 11(b) describes the 54 interferograms only selected by the traditional method with an average variance (i.e., red line)

FIGURE 13. *(Continued.)* Comparison of the time series displacements of the 27 GPS stations using the proposed method (red triangles on the left) and the traditional method (red triangles on the right): Gray dots represent the corresponding GPS time series results projected on the LOS direction.

of 44.69mm. Clearly, the variance of interferograms selected by the proposed method is lower and the average variance improves by 63.26%. This result also indicates that the traditional SBAS-InSAR method misses several high-quality interferograms with unfavourable spatial-temporal baselines and selected low-quality interferograms.

According to Equation (19), the mean velocities in Figs. 12(a) and (b), can be obtained on the basis of

the selected two different interferograms (i.e., Figs. 10(c) and (d)). Figs. 12 (a) and (b) show little differences. To better validate the proposed method, Fig. 13 shows the time series displacements of selected 27 GPS stations (i.e., blue triangles and dots in Figs. 12 (a) and (b)) from the two methods.

Fig. 13 shows several differences between the time series estimations from the proposed and the traditional methods. For quantitative comparison, the GPS measurement is
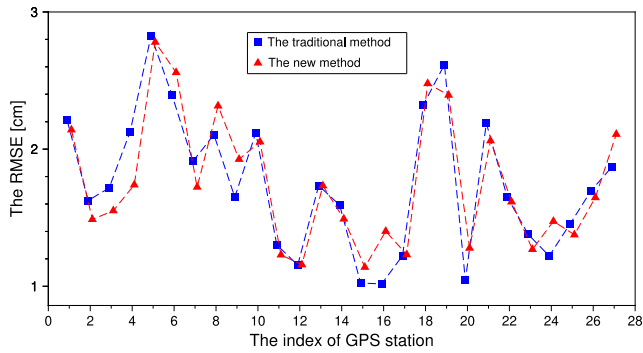
FIGURE 14. Comparison of RMSEs of the traditional spatial-temporal baseline threshold method (blue rectangles) and the proposed method (red triangles) for the 27 GPS stations.
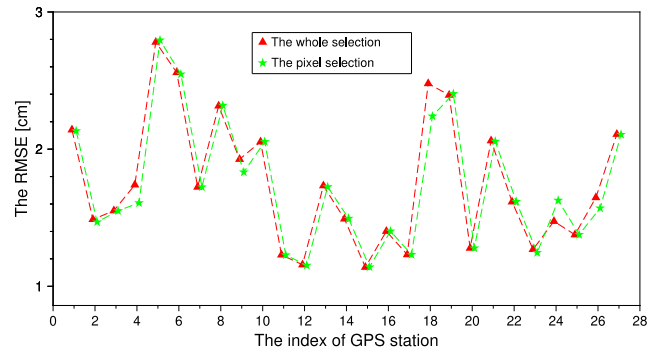
FIGURE 16. Comparison of the RMSE of the 27 GPS stations using the entire interferogran selection method (red triangles) and the pixel selection method (green triangles).
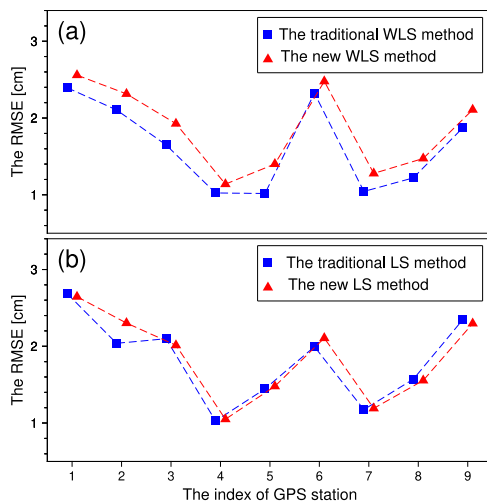

FIGURE 15. Comparison of RMSEs of the nine GPS stations (i.e., blue dots in Fig. 12) under the weighted (i.e., (a)) and unweighted (i.e., (b)) method: Blue rectangles and red triangles represent the traditional spatial-temporal baseline threshold method and the proposed method, respectively. The nine GPS station are BLBP, KEAW, KHKU, MLSP, MOKP, NUPM, PHAN, SLPC and YEEP.

regarded as truth and the RMSE of the two methods are calculated. Fig. 14 shows the comparison result more intuitively.

Fig. 14 shows that the RMSE under the proposed method is smaller than that of the traditional method. Meanwhile, the average RMSEs of the proposed and traditional methods are 1.75 and 1.76 cm, respectively. These results indicate the 0.57% improvement of the proposed method. However, nine GPS stations (i.e., BLBP, KEAW, KHKU, MLSP, MOKP, NUPM, PHAN, SLPC and YEEP) show that the RMSE under the proposed method is larger than the tradition method. This result may be caused by the weighted least squares (WLS) instead of least squares (LS). In other words, weighting limits the influence of low-quality interferograms selected by the traditional method on the displacement result. To illustrate this limit, Fig. 15 compares the results of these GPS stations in Fig. 12 (b) under the unweighted method.

Fig. 15 (a) shows that the RMSEs of the nine GPS stations are larger under the proposed interferogram selection

method. The maximum difference is 0.38 cm compared with the traditional interferogram selection method using the WLS approach. However, on the whole, the proposed method results are almost same as the traditional method under the LS algorithm in Fig. 15 (b). Combining Figs. 15 (a) and (b), a reasonable weighting method can help minimize the impact of interferograms with large variances, namely, low-quality interferograms. However, perfectly weighting each pixel in SBAS-InSAR is beyond the scope of this study. Meanwhile, notably, five GPS stations show better performance in the traditional method under the unweighted method. This result is further explained in the next section.

V. DISCUSSION

Fig. 15 (b) shows that the performance of the proposed method has larger RMSE in a few of GPS stations compared with the traditional method. The first reason may be due to the proposed method basing on the variance of entire interferogram instead of each pixel. In other words, selecting interferograms for each pixel in SBAS-InSAR is more reasonable than basing only on the entire interferogram. Therefore, interferograms are selected for the 27 GPS stations and the time series displacement is calculated for each station under the corresponding interferograms. Then, Fig. 16 shows the RMSE of 27 GPS stations under the full interferogram selection (red triangles) and the pixel selection method (green stars). Apparently, the pixel selection method performs slightly better than the entire interferogram selection method on the 27 GPS stations, except for the SLPC station. However, as the interferograms must be selected for each GPS station, the amount of time is approximately 27 times spent by each pixel selection method compared with the entire interferogram selection method. Similarly, our study area has 21629301, and the pixel selection method spends time that is approximately 21629301 times more than the entire interferogram selection method. Therefore, comparing the time cost and improvement accuracy, this study selects interferograms for SBAS-InSAR using the entire variance of each interferogram instead of the variance of each pixel.

Fig. 16 shows that using the pixel selection method, one GPS station (i.e., SLPC) has an RMSE that is larger than

the entire interferogram selection method. This result may be caused by the weighting method mentioned in Section IV that requires further study [15], [16]. However, weighting is beyond the current scope and therefore can be explored in the future.

VI. CONCLUSIONS

In this study, a novel adaptive optimization method for SBAS-InSAR based on MST algorithm and the turbulence atmosphere variance of each interferogram is proposed. Compared with the traditional interferogram selection approach, the proposed method is adaptive instead of prior to set spatial-temporal baseline thresholds from experience of the study area. This proposed method highly contributes to the automatic application of SBAS-InSAR measurement in engineering.

Moreover, the proposed method detects and eliminates the outliers of SLC images before inclusion in SBAS-InSAR calculation, a point that is not considered in traditional method. Furthermore, the proposed method can select high-quality interferograms that are missed due to unreasonable spatial-temporal baseline thresholds and delete low-quality interferograms affected by atmosphere and decorrelation noise that may be selected by the traditional method. Based on these reasons, the proposed method selects all of the interferograms that contains as little noise as possible from the non-outliers of SLC images to improve the measurement accuracy of SBAS-InSAR. The simulation and real data experiments at Hawaii demonstrate the superiority of the proposed method in improving the measurement accuracy of SBAS-InSAR.

ACKNOWLEDGMENT

REFERENCES

[1] Z. Li, Y. Cao, J. Wei, M. Duan, L. Wu, J. Hou, and J. Zhu, "Time-series InSAR ground deformation monitoring: Atmospheric delay modeling and estimating," *Earth-Sci. Rev.*, vol. 192, pp. 258–284, May 2019.

[2] P. Mateus, P. M. A. Miranda, G. Nico, J. Catalão, P. Pinto, and R. Tomé, "Assimilating InSAR maps of water vapor to improve heavy rainfall forecasts: A case study with two successive storms," *J. Geophys. Res., Atmos.*, vol. 123, no. 7, pp. 3341–3355, Apr. 2018.

[3] M. Duan, B. Xu, Z. Li, Y. Cao, J. Hu, W. Xu, J. Wei, and G. Feng, "Non-differential water vapor estimation from SBAS-InSAR," *J. Atmos. Solar-Terr. Phys.*, vol. 204, Aug. 2020, Art. no. 105284.

[4] Y. Du, L. Zhang, G. Feng, Z. Lu, and Q. Sun, "On the accuracy of topographic residuals retrieved by MTInSAR," *IEEE Trans. Geosci. Remote Sens.*, vol. 55, no. 2, pp. 1053–1065, Feb. 2017.

[5] R. Lanari, P. Berardino, M. Bonano, F. Casu, A. Manconi, M. Manunta, M. Manzo, A. Pepe, S. Pepe, E. Sansosti, G. Solaro, P. Tizzani, and G. Zeni, "Surface displacements associated with the L'Aquila 2009 Mw 6.3 earthquake (central Italy): New evidence from SBAS-DInSAR time series analysis," *Geophys. Res. Lett.*, vol. 37, no. 20, pp. 1–6, Oct. 2010.

[6] M. Cho, L. Zhang, and C.-W. Lee, "Monitoring of volcanic activity of augustine volcano, alaska using TCPInSAR and SBAS time-series techniques for measuring surface deformation," *Korean J. Remote Sens.*, vol. 29, no. 1, pp. 21–34, Feb. 2013.

[7] C. Zhao, Y. Kang, Q. Zhang, Z. Lu, and B. Li, "Landslide identification and monitoring along the jinsha river catchment (Wudongde reservoir Area), China, using the InSAR method," *Remote Sens.*, vol. 10, no. 7, p. 993, Jun. 2018.

[8] R. Zhao, Z.-W. Li, G.-C. Feng, Q.-J. Wang, and J. Hu, "Monitoring surface deformation over permafrost with an improved SBAS-InSAR algorithm: With emphasis on climatic factors modeling," *Remote Sens. Environ.*, vol. 184, pp. 276–287, Oct. 2016.

[9] L. Zhou, J. Guo, J. Hu, J. Li, Y. Xu, Y. Pan, and M. Shi, "Wuhan surface subsidence analysis in 2015–2016 based on Sentinel-1a data by SBAS-InSAR," *Remote Sens.*, vol. 9, no. 10, p. 982, 2017.

[10] J. Hu, Z. Li, X. Ding, J. Zhu, and Q. Sun, "Spatial–temporal surface deformation of los angeles over 2003–2007 from weighted least squares DInSAR," *Int. J. Appl. Earth Observ. Geoinf.*, vol. 21, pp. 484–492, Apr. 2013.

[11] Z. Yang, Z. Li, J. Zhu, G. Feng, Q. Wang, J. Hu, and C. Wang, "Deriving time-series three-dimensional displacements of mining areas from a single-geometry InSAR dataset," *J. Geodesy*, vol. 92, no. 5, pp. 529–544, May 2018.

[12] C. De Luca, R. Cuccu, S. Elefante, I. Zinno, M. Manunta, V. Casola, G. Rivolta, R. Lanari, and F. Casu, "An on-demand Web tool for the unsupervised retrieval of Earth's surface deformation from SAR data: The P-SBAS service within the ESA G-POD environment," *Remote Sens.*, vol. 7, no. 11, pp. 15630–15650, Nov. 2015.

[13] S. V. Samsonov and N. d'Oreye, "Multidimensional small baseline subset (MSBAS) for two-dimensional deformation analysis: Case study mexico city," *Can. J. Remote Sens.*, vol. 43, no. 4, pp. 318–329, Jul. 2017.

[14] M. P. Doin, S. Guillaso, R. Jolivet, C. Lasserre, F. Lodge, G. Ducret, and R. Grandin, "Presentation of the small baseline NSBAS processing chain on a case example: The Etna deformation monitoring from 2003 to 2010 using Envisat data," in *Proc. Fringe Symp. (ESA)*, 2011, pp. 3434–3437.

[15] L. Bateson, F. Cigna, D. Boon, and A. Sowter, "The application of the intermittent SBAS (ISBAS) InSAR method to the South Wales coalfield, UK," *Int. J. Appl. Earth Observ. Geoinf.*, vol. 34, pp. 249–257, Feb. 2015.

[16] E. S. Samiei, "Exploitation of distributed scatterers in synthetic aperture radar interferometry," Ph.D. dissertation, Delft Univ. Technol., Delft, The Netherlands, 2017.

[17] P. J. González and J. Fernández, "Error estimation in multitemporal InSAR deformation time series, with application to Lanzarote, Canary Islands," *J. Geophys. Res.*, vol. 116, no. B10, 2011.

[18] P. S. Agram and M. Simons, "A noise model for InSAR time series," *J. Geophys. Res., Solid Earth*, vol. 120, no. 4, pp. 2752–2771, Apr. 2015.

[19] Y. Cao, Z. Li, J. Wei, J. Hu, M. Duan, and G. Feng, "Stochastic modeling for time series InSAR: With emphasis on atmospheric effects," *J. Geodesy*, vol. 92, no. 2, pp. 185–204, Feb. 2018.

[20] M. Jiang and A. M. Guarnieri, "Distributed scatterer interferometry with the refinement of spatiotemporal coherence," *IEEE Trans. Geosci. Remote Sens.*, vol. 58, no. 6, pp. 3977–3987, Jun. 2020.

[21] R. Torres *et al.*, "GMES Sentinel-1 mission," *Remote Sens. Environ.*, vol. 120, pp. 9–24, May 2012.

[22] F. Casu, M. Manunta, P. S. Agram, and R. E. Crippen, "Big remotely sensed data: Tools, applications and experiences," *Remote Sens. Environ.*, vol. 202, pp. 1–2, Dec. 2017.

[23] P. Berardino, G. Fornaro, R. Lanari, and E. Sansosti, "A new algorithm for surface deformation monitoring based on small baseline differential SAR interferograms," *IEEE Trans. Geosci. Remote Sens.*, vol. 40, no. 11, pp. 2375–2383, Nov. 2002.

[24] R. F. Hanssen, *Radar Interferometry: Data Interpretation and Error Analysis*. Springer, 2001.

[25] A. M. Guarnieri and S. Tebaldini, "Hybrid Cramér–Rao bounds for crustal displacement field estimators in SAR interferometry," *IEEE Signal Process. Lett.*, vol. 14, no. 12, pp. 1012–1015, Dec. 2007.

[26] B. Xu, Z. Li, Y. Zhu, J. Shi, and G. Feng, "SAR interferometric baseline refinement based on flat-Earth phase without a ground control point," *Remote Sens.*, vol. 12, no. 2, p. 233, Jan. 2020.

[27] W. B. Xu, Z. W. Li, X. L. Ding, and J. J. Zhu, "Interpolating atmospheric water vapor delay by incorporating terrain elevation information," *J. Geodesy*, vol. 85, no. 9, pp. 555–564, 2012.

[28] P. Teunissen, D. J. Simons, and C. Tiberius, *Probability and Observation Theory*. Delft, The Netherlands: Delft Univ. of Technology, 2004.

[29] N. Cressie, "Statistics for spatial data," *Terra Nova*, vol. 4, no. 5, pp. 613–617, 1992.

[30] H. A. Zebker and J. Villasenor, "Decorrelation in interferometric radar echoes," *IEEE Trans. Geosci. Remote Sens.*, vol. 32, no. 4, pp. 823–836, Sep. 2002.

[31] D. Just and R. Bamler, "Phase statistics of interferograms with applications to synthetic aperture radar," *Appl. Opt.*, vol. 33, no. 20, pp. 4361–4368, 1994.

[32] E. Rodriguez and J. M. Martin, "Theory and design of interferometric synthetic aperture radars," *IEE Proc. F-Radar Signal Process.*, vol. 139, no. 2, pp. 147–159, Apr. 1992.

[33] E. C. Reinisch, M. Cardiff, and K. L. Feigl, "Graph theory for analyzing pair-wise data: Application to geophysical model parameters estimated from interferometric synthetic aperture radar data at Okmok volcano, Alaska," *J. Geodesy*, vol. 91, no. 1, pp. 9–24, 2018.

[34] A. Refice, F. Bovenga, and R. Nutricato, "MST-Based stepwise connection strategies for multipass radar data, with application to coregistration and equalization," *IEEE Trans. Geosci. Remote Sens.*, vol. 44, no. 8, pp. 2029–2039, Jul. 2006.

[35] T. Wang, D. Perissin, F. Rocca, and M.-S. Liao, "Three gorges dam stability monitoring with time-series InSAR image analysis," *Sci. China Earth Sci.*, vol. 54, no. 5, pp. 720–732, May 2011.

[36] J.-H. Liu, J. Hu, Z.-W. Li, J.-J. Zhu, Q. Sun, and J. Gan, "A method for measuring 3-D surface deformations with InSAR based on strain model and variance component estimation," *IEEE Trans. Geosci. Remote Sens.*, vol. 56, no. 1, pp. 239–250, Jan. 2018.

[37] Z. W. Li, X. L. Ding, C. Huang, D. W. Zheng, W. B. Zou, and Y. K. Shea, "Filtering method for SAR interferograms with strong noise," *Int. J. Remote Sens.*, vol. 27, no. 14, pp. 2992–3000, 2006.

[38] C. W. Chen and H. A. Zebker, "Two-dimensional phase unwrapping with use of statistical models for cost functions in nonlinear optimization," *J. Opt. Soc. Amer. A, Opt. Image Sci.*, vol. 18, no. 2, pp. 338–351, 2001.

MENG DUAN received the master's degree in surveying engineering from Central South University, Changsha, China, in 2016, where she is currently pursuing the Ph.D. degree in geophysics and geodesy. Her research interests include estimation theory and advanced processing developments for multi-temporal synthetic aperture interferometry and deformation monitoring.

BING XU received the bachelor's and Ph.D. degrees in surveying engineering from Central South University, Changsha, China, in 2011 and 2016, respectively. He is currently a Teacher with the Department of Surveying and Remote Sensing, School of Geoscience and Info-Physics, Central South University. His research interests include interferometric synthetic aperture radar for inverting source parameters of earthquakes and ground deformation monitoring in urban areas.

ZHI-WEI LI received the bachelor's and master's degrees in surveying engineering from the Central South University of Technology (currently Central South University), Changsha, China, in 1997 and 1999, respectively, and the Ph.D. degree in remote sensing from The Hong Kong Polytechnic University, Hong Kong, in 2005.

WEN-HAO WU received the Ph.D. degree in photogrammetry and remote sensing from Wuhan University, Wuhan, China, in 2016. He is currently a Teacher with the Hunan Province Key Laboratory of Coal Resources Clean-utilization and Mine Environment Protection, Hunan University of Science and Technology.

JIAN-CHAO WEI received the master's degree in surveying engineering and the Ph.D. degree in geophysics and geodesy from Central South University, Changsha, China, in 2007 and 2018, respectively. He is currently a Teacher with the Hunan Province Key Laboratory of Coal Resources Clean-utilization and Mine Environment Protection, Hunan University of Science and Technology. His main research interests include statistical signal processing, synthetic aperture radar processing, and atmospheric physics.

YUN-MENG CAO received the Ph.D. degree in surveying engineering from Central South University, Changsha, China, in 2018. He is currently pursuing the Ph.D. degree with the King Abdullah University of Science and Technology. His current research interests include atmospheric remote sensing application and spatial-temporal analysis.

JI-HONG LIU received the bachelor's degree from the School of Geosciences and Info-Physics, Central South University, Changsha, China, in 2017, where he is currently pursuing the Ph.D. degree in geodesy and surveying engineering. His current research interests include interferometric synthetic aperture radar and its applications to 3-D surface deformation mapping.

• • •